

The amorphous-structure conundrum in two-dimensional materials: Monolayer amorphous carbon *versus* boron nitride

Yu-Tian Zhang (张雨田)^{1#}, Yun-Peng Wang (王云鹏)^{2#}, Xianli Zhang (张现利)¹,
Yu-Yang Zhang (张余洋)^{1,3*}, Shixuan Du (杜世萱)^{1,4}, Sokrates T. Pantelides^{5,1}

- 1 University of Chinese Academy of Sciences and Institute of Physics, Chinese Academy of Sciences, Beijing 100049, China
- 2 Hunan Key Laboratory for Super Microstructure and Ultrafast Process, School of Physics and Electronics, Central South University, Changsha 410083, China
- 3 CAS Center for Excellence in Topological Quantum Computation, University of Chinese Academy of Sciences, Beijing 100049, China
- 4 Songshan Lake Materials Laboratory, Dongguan, Guangdong 523808, China
- 5 Department of Physics and Astronomy and Department of Electrical and Computer Engineering, Vanderbilt University, Nashville, Tennessee 37235, USA

Abstract

The structure of amorphous materials – continuous random networks (CRN) *vs.* CRN containing randomly dispersed crystallites – has been debated for decades. In two-dimensional (2D) materials, this question can be addressed more directly. Recently, controlled experimental conditions and atomic-resolution imaging found that monolayer amorphous carbon (MAC) is a CRN containing random graphene nanocrystallites. Here we report Monte Carlo simulations of the structure evolution of monolayer amorphous boron nitride (ma-BN) and demonstrate that it also features distorted sp^2 -bonding, but it has a purely CRN structure. The key difference is that, at low temperatures, C atoms easily form hexagons, whereas the probability to form canonical B-N-B-N-B-N hexagons is very low. On the other hand, hexagons have lower energy than non-hexagons, which results in *hexagonal CRN* regions that grow much like nanocrystallites in MAC. The net conclusion is that two distinct forms of amorphous structure are possible in 2D materials. The as-generated ma-BN is stable at room-temperature and insulating.

Introduction

Amorphous materials, unlike their crystalline counterparts, have no long-range order. They have rich applications: hydrogenated amorphous silicon (a-Si:H) has been used in photovoltaics and thin-film transistors in liquid-crystal displays [1]; amorphous SiO₂ (a-SiO₂) is a key material in microelectronics and chromatography [2,3]; and amorphous metal-oxide semiconductors like indium-gallium-zinc oxide (IGZO) is used for thin-film transistors in organic light-emitting diode displays [4-6]. Crystalline structures can be detected by X-ray diffraction and other techniques, while the atomic structure of amorphous materials has long been the subject of intense study and debate [7-11].

There are two major competing models for the microscopic structure of amorphous materials. The continuous-random-network (CRN) model, proposed by Zachariasen [12] in 1932, posits that the local arrangement of atoms in amorphous materials is similar to that in the corresponding crystalline structure, but the bond-angles vary and the long-range order is absent. The “crystallite model”, proposed earlier by Lebedev [13], posits that amorphous materials are CRNs with randomly dispersed crystallites. Amorphous SiO₂ has long been viewed as a prototype for the CRN model. By the late 1980’s, it was settled that a-Si is also a CRN, but the debate was revived in 2010 by new imaging techniques and simulations [9,10,14].

The same question arises about the structure of amorphous two-dimensional (2D) materials, but it can be addressed by experiments more directly because unobscured atomic-resolution imaging of their structure is possible. For graphene, the prototypical 2D material, early works employed an electron microscope’s electron beam to introduce defects that gradually evolve into disordered regions and ultimately a fully disordered monolayer that may contain holes because carbon atoms are ejected during continued exposure to the electron beam [15,16]. This approach, however, can intentionally eliminate all remaining graphene crystallites, leaving open the question of the intrinsic nature of amorphous 2D materials. More recently, controlled synthesis and atomic-level imaging of monolayer amorphous carbon (MAC) was achieved [17], clearly showing that the structure of MAC is a CRN containing dispersed distorted nanocrystallites that could not be avoided by varying the growth process. For other single-atom-thick 2D materials such as monolayer hexagonal boron nitride (h-BN), the amorphous phase remains largely unexplored. Wu et al. calculated the thermal conductivity of monolayer h-BN in which they introduced an increasing number of defects (vacancies, divacancies, and Stone-Wales defects) reaching the amorphous limit [18]. As in the case of electron-beam-induced disordering, this approach to amorphization allows one to eliminate crystallites at will, leaving unanswered the question about the structure of as-synthesized amorphous 2D materials. Experimentally, amorphous BN thin films with a thickness of 2-17 nm have been successfully synthesized by chemical vapor deposition (CVD) [19,20], but their atomic structure was not characterized in detail. The successful synthesis of thin-film amorphous BN enhances the interest in its monolayer analog, whose existence and atomic structure are unknown. It can also serve as a test of the universality of the atomic structure of amorphous monolayers and potentially offer insights into the structure of amorphous 3D materials.

In this paper, we report Monte Carlo simulations of the growth of monolayer amorphous BN (ma-BN) and compare the results to those of corresponding simulations for MAC, as reported in Ref. [17]. We use empirical potentials complemented by density-functional-theory (DFT) accuracy tests for critical quantities. As in Ref. [17], we find that randomly distributed C atoms quickly acquire threefold coordination and

form hexagons and distorted graphene-like crystallites that grow in size with continued annealing. Nanocrystalline and even crystalline graphene can be obtained after long-time simulations. In sharp contrast, randomly distributed B and N atoms, though they also quickly acquire threefold coordination and form hexagons and other polygons, with very rare exceptions, these polygons are not canonical, i.e., they do not feature alternating B and N atoms. We do not observe formation of h-BN crystallites no matter how long the simulation time. It is the binary nature of BN that generates insurmountable steric constraints for the formation of canonical hexagons and hence h-BN crystallites. On the other hand, because hexagons are always lower in energy than all other polygons, we find that *hexagonal CRN (h-CRN)* regions, comprising noncanonical hexagons, which is a unique feature of binary honeycomb-structured monolayers, grow very much like nanocrystallites grow in MAC. Finally, ma-BN features a small number of B_3 triangles that are reminiscent of borophene. The effect of amorphization on the electronic properties are studied. A graphene/ma-BN heterostructure is also studied. Finally, the generality of the conclusions in other amorphous 2D materials and its applicability to 3D materials are discussed.

Results and discussion

We employed a kinetic Monte Carlo (kMC) algorithm as in Refs. [17,21,22] to simulate the formation of amorphous materials as an annealing process. We used the BN-ExTeP empirical potentials for BN, which were tested extensively in Ref. [23]. Additional tests for atomic rearrangements commonly encountered in our algorithm are described in Supplemental Material (Tables S1 and S2). First we performed kMC simulations of the atomic structure of MAC using the potentials of Ref. [24]. Starting with randomly distributed carbon atoms, hexagons and graphene nanocrystals form quickly in the early stages, as shown in the nucleation state (Fig. 1b), because hexagons have lower energies than other structural units [25-30]. The nanocrystals are embedded in a 2D CRN of threefold-coordinated C atoms and continue to grow as the “annealing” continues as shown in Fig. 1c, which is consistent with the crystallite model of MAC [17]. Continuing annealing leads to an ever-increasing number of carbon hexagons, while the crystallites merge to form polycrystalline graphene with only two crystalline orientations in the simulation box. At the final stage of the simulation, the grain boundary is eliminated, and a continuous sheet of graphene with some defects is obtained (Fig. S1). Though it is possible for the kMC algorithm to ultimately lead to pure graphene, in a real annealing process, e.g., by quantum MD, steric constraints may make the elimination of isolated monovacancies all but impossible (see e.g., a monovacancy near the left boundary in Fig. S1c that persists in Fig. S1d). The message here from the kMC algorithm, which does not contain a real temperature, is that pristine crystalline graphene can more easily grow at an appropriate growth temperature as opposed to annealing MAC (see Fig. S1i, showing that the kMC-evolving energy of

MAC saturates above the energy of pristine graphene).

The same kMC algorithm is employed to generate atomic structures of ma-BN. Starting from an initial configuration with randomly arranged boron and nitrogen atoms (Fig. 1e), threefold coordination is again achieved rapidly as sp^2 bonding is energetically preferred by both B and N. Noncanonical BN hexagons and other polygons that lack an alternation of B and N atoms form quickly and persist. Isolated canonical BN hexagons with alternating B-N appear and disappear randomly no matter how long we run the simulation, even after the total energy reaches a stable value (Fig. S1). In contrast, the number of noncanonical hexagons continues to grow and stabilizes as the total energy converges (Fig. 1f-h). h-BN crystallites never form, whereby we conclude that ma-BN has a purely CRN structure, in stark contrast to the MAC.

The structural difference between MAC and ma-BN originates from the binary nature of BN. The presence of only C atoms in MAC means that there are only C-C bonds, whereby all the hexagons are automatically canonical. The dominant factor in the kMC for MAC is the energy competition between carbon hexagons and non-hexagons. The lower-energy hexagons prevail quickly and form crystallites that keep growing with extended annealing. In the ma-BN case, on the other hand, more subtle energy competitions need to be considered: (1) hexagon vs. non-hexagon as in the MAC case and (2) canonical vs. noncanonical hexagons, which is unique to ma-BN. Competition (2) is governed by the relative energies of canonical B-N bonds and noncanonical B-B and N-N bonds (noncanonical-bond energies are compared with DFT results in Table S2). In ma-BN, the B-B and N-N noncanonical bonds lead to noncanonical BN hexagons, which have lower energies than the other noncanonical polygons, but higher energies than canonical hexagons. Thus the kMC process can drive non-hexagons to noncanonical hexagons as well. As an upper bound, we calculated the probability of forming a canonical BN hexagon to be 10% of the unity bonding probability in MAC (see Fig. S3 for details). The aforementioned two types of energy competitions impose an insurmountable steric constraint on the formation of canonical BN hexagons, which explains why h-BN crystallites do not form.

The energy evolution of the kMC simulation is shown in Fig. 2a. The total energy converges after \sim 180,000 kMC steps. The snapshot at the 180,000th step is chosen as the representative configuration of ma-BN in all subsequent discussions. Moreover, the converged energy of ma-BN is about 100 meV/atom higher than that of h-BN, which is similar to the carbon case (the total energy of a MAC is \sim 130 meV/atom higher than that of graphene). The higher energy than h-BN reflects the metastability of ma-BN. Meanwhile, the thermodynamic stability of ma-BN is confirmed by classical MD simulations at 300 K. As shown in Fig. 2b, there is no sudden change in the total energy after equilibration. The energy fluctuation is \sim 10 meV/atom for both h-BN and ma-BN, smaller than $k_B T \sim 26$ meV at room temperature, reflecting the energetic stability. There

are only minor structural changes in terms of bond-lengths and bond-angles after a long-time 10 ns MD simulation, while the large thermal corrugation does not destroy the overall topological structure (Fig. S4), confirming the structural stability.

A detailed analysis of the structural features of ma-BN is shown in Fig. 3. In a representative snapshot (Fig. 3a), the dominating noncanonical BN hexagons form continuous regions or “grains” (blue regions in Fig. 1g and Fig. 3a), which contribute about 63% of all structural units in our prototype equilibrated sample (Fig. S5). We call the structure of these regions *hexagonal CRN (h-CRN)* and note the geometrical analogy with nanocrystalline graphene. The h-CRN is a unique feature in binary and multi-component amorphous materials. On the other hand, canonical BN hexagons are rare and isolated, as mentioned earlier. The secondary dominant structural unit is the pentagon-heptagon pairs (5/7 pairs), which contribute $\sim 31\%$ of the total structural units (Fig. S5). The 5/7 pairs also form boundaries (yellow-orange regions in Fig. 3a) that separate the h-CRN regions. The four- and eight-membered rings (4/8) contribute little ($\sim 1.6\%$). The B_3 triangles in ma-BN are structural elements of borophene but they contribute only 2.7%. Note that B_3 triangles still form in a nitrogen rich environment (Fig. S6), further confirming their robust nature.

The calculated radial distribution function (RDF) (Fig. 3b) shows that the middle- and long-range RDF peaks of ma-BN are highly broadened or lost, while the short-range peaks are basically preserved. Specifically, the first RDF peak at around 1.5 Å represents the nearest-neighbor coordination. N-N and B-N bonds contribute to the first subpeak at 1.41 Å, while B-B bonds contribute to the second subpeak at 1.54 Å (Fig. 3c). The broad subpeaks reveal bond-length variations. The dominant threefold coordination (Fig. 3d) is driven by sp^2 bonding. A broad peak near 120° in the bond angle counting (Fig. 3e) reflects the existence of a substantial number of distorted noncanonical hexagons and other polygons. The small distribution of bond angles near 60° and 180° are contributed by B_3 triangles and eight-/nine-rings, respectively. Combining the threefold coordination and the bond length/angle variations, we conclude that the bonding nature of ma-BN is a distorted sp^2 -bonding. All of Zachariasen’s requirements for a 2D glass [12,31] are satisfied by ma-BN, establishing ma-BN as a true Z-CRN.

Next, we study the electronic structure of ma-BN. Figure 4a shows the electronic density of states (DOS) of ma-BN. Different from h-BN, which has a large band-gap, there is a continuum of in-gap states for ma-BN. However, the charge densities of the gap states near the Fermi energy are localized mainly at the boundary formed by 5/7 pairs (Fig. 4b). These electronic states are disconnected so that they cannot conduct current – ma-BN is insulating (Fig. S7).

We also tested the possibility of ma-BN being one component in a 2D van der Waals heterostructure. We consider a vertical Gr/ma-BN heterostructure. After DFT

structural optimization, the average interlayer distance is 4.2 Å, which is about 24% larger than that of Gr/h-BN heterostructure (~ 3.4 Å). The calculated DOS and charge density distribution of the heterostructure is shown in Fig. 4c and 4d. The charge density near the Fermi energy is mainly localized in the 5/7 boundaries of the ma-BN, but the shape of the Dirac cone of graphene is intact, indicating that the heterostructure is conducting. Comparing to a Gr/h-BN heterostructure where the graphene Dirac point locates right at the Fermi level, the Dirac point is shifted by -0.14 eV in Gr/ma-BN, indicating that the graphene layer is *n*-doped.

Conclusions

In summary, we predicted the atomic structure of amorphous monolayer BN as a Z-CRN. The difference with monolayer amorphous carbon is caused by the low probability of forming canonical BN hexagons imposed by the additional steric constraint created by the two atomic species. We found, however, yet another intriguing feature of ma-BN. The noncanonical hexagons in ma-BN have lower energy than other polygons and quickly form nanoregions of what we call hexagonal CRN. These nanoregions are analogs of nanocrystallites in MAC and also grow in size with continuing annealing. The possibility of growing a purely h-CRN ma-BN comprising only noncanonical hexagons is small, however, as Figs. S1g and S1h reveal. Just like MAC is unlikely to yield pristine graphene by annealing because of steric constraint, the same way steric constrains would prohibit an all h-CRN ma-BN.

The ma-BN is structurally and thermodynamically stable at room temperature. The disappearance of long-range order and preservation of short-range coordination establishes the structure to be truly amorphous. As an insulating monolayer with good stability at room-temperature, ma-BN may be suitable for similar applications as monolayer amorphous carbon [17,31].

The generality of the ma-BN results and the implications for other two- and three-dimensional amorphous compounds cannot be fully resolved at this point. Our simulation results strongly suggest that, like MAC, amorphous single-element monolayers are likely to feature crystallites embedded in a CRN, whereas amorphous binary and other compound monolayers are likely to form pure CRNs with noncanonical hexagons and other polygons. The formation of noncanonical bonding in a binary monolayer is inevitable and more likely than the formation of canonical bonding. However, due to the lack of adequately reliable empirical potentials for some of the most typical 2D materials like borophene, monolayer GaAs and monolayer BeO, our conclusion on the distinction between single-element and binary amorphous materials remains to be confirmed. Furthermore, the distinction between single-element and binary materials may extend to bulk materials. For example, bulk amorphous Si, being a single-element material, may well contain crystallites that nucleate by thermal fluctuations but cannot grow large under the growth conditions [10,14]. Such crystallites are far less likely in binary amorphous materials, e.g., a-SiC [32-35].

Acknowledgements

We acknowledge financial support from National Key R&D program of China (Nos. 2019YFA0308500, 2018YFA0305800, and 2016YFA0202300), National Natural Science Foundation of China (Nos. 51922011, 61888102, 12004439), Strategic Priority Research Program of the Chinese Academy of Sciences (Nos. XDB30000000 and XDB28000000), the K. C. Wong Education Foundation, and the Fundamental Research Funds for the Central Universities. Work at Vanderbilt was funded by the U.S. Department of Energy, Office of Science, Basic Energy Sciences, Materials Science and Engineering Division grant no. DE-FG02-09ER46554 and by the McMinn Endowment.

References

- [1] P. G. Lecomber, Present and future applications of amorphous-silicon and its alloys, *J. Non-Cryst. Solids* **115**, 1 (1989).
- [2] J. P. C. Vissers, H. A. Claessens, and C. A. Cramers, Microcolumn liquid chromatography: Instrumentation, detection and applications, *J. Chromatogr. A* **779**, 1 (1997).
- [3] D. A. Muller, T. Sorsch, S. Moccio, F. H. Baumann, K. Evans-Lutterodt, and G. Timp, The electronic structure at the atomic scale of ultrathin gate oxides, *Nature* **399**, 758 (1999).
- [4] J. K. Jeong, J. H. Jeong, H. W. Yang, J.-S. Park, Y.-G. Mo, and H. D. Kim, High performance thin film transistors with cosputtered amorphous indium gallium zinc oxide channel, *Appl. Phys. Lett.* **91**, 113505 (2007).
- [5] J.-S. Park, J. K. Jeong, Y.-G. Mo, H. D. Kim, and S.-I. Kim, Improvements in the device characteristics of amorphous indium gallium zinc oxide thin-film transistors by Ar plasma treatment, *Appl. Phys. Lett.* **90**, 262106 (2007).
- [6] J. K. Jeong, The status and perspectives of metal oxide thin-film transistors for active matrix flexible displays, *Semicond. Sci. Technol.* **26**, 034008 (2011).
- [7] V. L. Deringer, N. Bernstein, G. Csanyi, C. Ben Mahmoud, M. Ceriotti, M. Wilson, D. A. Drabold, and S. R. Elliott, Origins of structural and electronic transitions in disordered silicon, *Nature* **589**, 59 (2021).
- [8] Y. Yang *et al.*, Determining the three-dimensional atomic structure of an amorphous solid, *Nature* **592**, 60 (2021).
- [9] S. Roorda and L. J. Lewis, Comment on “The local structure of amorphous silicon”, *Science* **338**, 1539 (2012).
- [10] M. Treacy and K. Borisenko, The local structure of amorphous silicon, *Science* **335**, 950 (2012).
- [11] A. C. Wright, The great crystallite versus random network controversy: A personal perspective, *Int. J. Appl. Glass Sci.* **5**, 31 (2014).
- [12] W. H. Zachariasen, The atomic arrangement in glass, *J. Am. Chem. Soc.* **54**, 3841 (1932).
- [13] A. Lebedev, On the polymorphism and annealing of glass, *Trudy Gos. Opt. Inst*

2, 1 (1921).

- [14] J. M. Gibson, M. M. Treacy, T. Sun, and N. J. Zaluzec, Substantial crystalline topology in amorphous silicon, *Phys. Rev. Lett.* **105**, 125504 (2010).
- [15] J. Kotakoski, A. V. Krasheninnikov, U. Kaiser, and J. C. Meyer, From point defects in graphene to two-dimensional amorphous carbon, *Phys. Rev. Lett.* **106**, 105505 (2011).
- [16] F. R. Eder, J. Kotakoski, U. Kaiser, and J. C. Meyer, A journey from order to disorder - atom by atom transformation from graphene to a 2D carbon glass, *Sci Rep* **4**, 4060 (2014).
- [17] C. T. Toh *et al.*, Synthesis and properties of free-standing monolayer amorphous carbon, *Nature* **577**, 199 (2020).
- [18] X. Wu and Q. Han, Thermal conductivity of monolayer hexagonal boron nitride: From defective to amorphous, *Comput. Mater. Sci.* **184**, 109938 (2020).
- [19] N. R. Glavin *et al.*, Amorphous boron nitride: A universal, ultrathin dielectric for 2D nanoelectronics, *Adv. Funct. Mater.* **26**, 2640 (2016).
- [20] S. Hong *et al.*, Ultralow-dielectric-constant amorphous boron nitride, *Nature* **582**, 511 (2020).
- [21] F. Ding and B. I. Yakobson, Energy-driven kinetic Monte Carlo method and its application in fullerene coalescence, *J. Phys. Chem. Lett.* **5**, 2922 (2014).
- [22] J. Zhuang, R. Zhao, J. Dong, T. Yan, and F. Ding, Evolution of domains and grain boundaries in graphene: A kinetic Monte Carlo simulation, *Phys. Chem. Chem. Phys.* **18**, 2932 (2016).
- [23] J. H. Los, J. M. H. Kroes, K. Albe, R. M. Gordillo, M. I. Katsnelson, and A. Fasolino, Extended Tersoff potential for boron nitride: Energetics and elastic properties of pristine and defective h-BN, *Phys. Rev. B* **96**, 184108 (2017).
- [24] S. J. Stuart, A. B. Tutein, and J. A. Harrison, A reactive potential for hydrocarbons with intermolecular interactions, *J. Chem. Phys.* **112**, 6472 (2000).
- [25] H. Shin, S. Kang, J. Koo, H. Lee, J. Kim, and Y. Kwon, Cohesion energetics of carbon allotropes: Quantum Monte Carlo study, *J. Chem. Phys.* **140**, 114702 (2014).
- [26] S. Zhang, J. Zhou, Q. Wang, X. Chen, Y. Kawazoe, and P. Jena, Penta-graphene: A new carbon allotrope, *Proc. Natl. Acad. Sci. U. S. A.* **112**, 2372 (2015).
- [27] X. Li, Q. Wang, and P. Jena, psi-Graphene: A new metallic allotrope of planar carbon with potential applications as anode materials for lithium-ion batteries, *J. Phys. Chem. Lett.* **8**, 3234 (2017).
- [28] B. Ram and H. Mizuseki, Tetrahexcarbon: A two-dimensional allotrope of carbon, *Carbon* **137**, 266 (2018).
- [29] S. Wang, B. Yang, H. Chen, and E. Ruckenstein, Popgraphene: a new 2D planar carbon allotrope composed of 5–8–5 carbon rings for high-performance lithium-ion battery anodes from bottom-up programming, *J. Mater. Chem. A* **6**, 6815 (2018).
- [30] W. Zhang, C. Chai, Q. Fan, Y. Song, and Y. Yang, PBCF-Graphene: A 2D sp^2 hybridized honeycomb carbon allotrope with a direct band gap, *ChemNanoMat*

6, 139 (2019).

- [31] W. J. Joo *et al.*, Realization of continuous Zachariasen carbon monolayer, *Sci. Adv.* **3**, e1601821 (2017).
- [32] M. Gorman and S. A. Solin, Direct evidence for homonuclear bonds in amorphous SiC, *Solid State Commun.* **15**, 761 (1974).
- [33] Y. Inoue, S. Nakashima, A. Mitsuishi, S. Tabata, and S. Tsuboi, Raman spectra of amorphous SiC, *Solid State Commun.* **48**, 1071 (1983).
- [34] M. Ishimaru, I. T. Bae, Y. Hirotsu, S. Matsumura, and K. E. Sickafus, Structural relaxation of amorphous silicon carbide, *Phys. Rev. Lett.* **89**, 055502 (2002).
- [35] V. I. Ivashchenko, P. E. A. Turchi, and V. I. Shevchenko, Simulations of the mechanical properties of crystalline, nanocrystalline, and amorphous SiC and Si, *Phys. Rev. B* **75**, 085209 (2007).

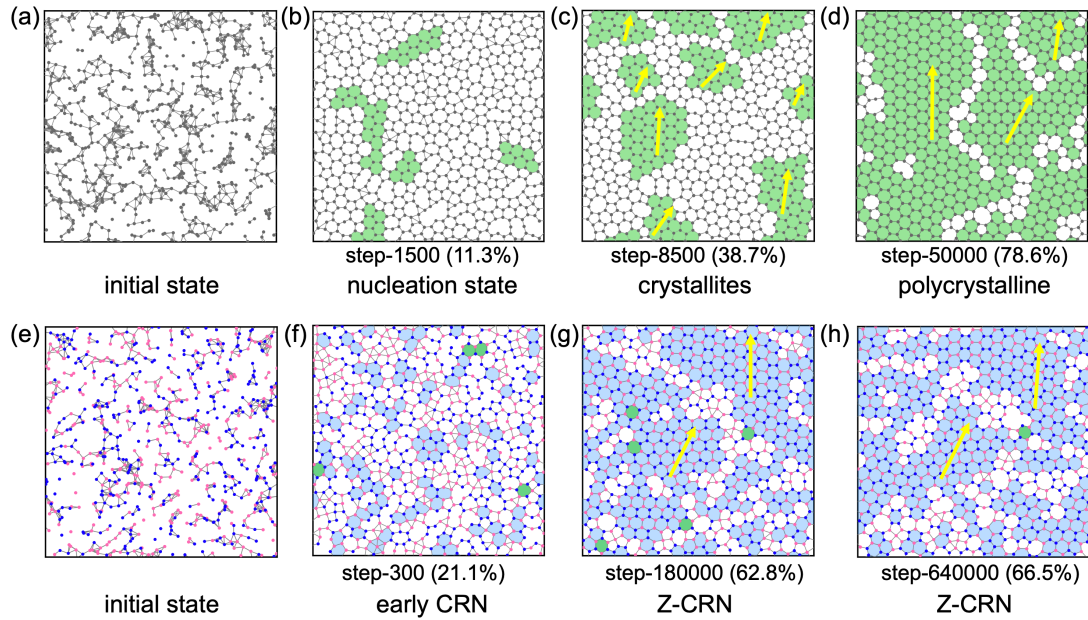


Fig. 1. Atomic structures of MAC and ma-BN in kMC annealing. (a)-(d) Four stages of MAC. (a) The initial configuration with randomly distributed carbon atoms. (b) Carbon hexagons, colored green, form quickly in the nucleation state; the percentage of hexagons in crystallites is listed in parentheses. (c) Several nanocrystallites form fairly quickly, with different orientations (yellow arrows). (d) Polycrystalline graphene at equilibrium stage. (e)-(h) Four stages of ma-BN. The h-CRN regions are colored blue, and their orientations are marked by yellow arrows. (e) Initial structure with randomly arranged boron and nitrogen atoms. (f) Early CRN stage; the percentage of noncanonical BN hexagons is listed in parentheses. (g) Equilibrium stage, which shows a Z-CRN structure. (h) Long-time post-equilibrium stage. Note the similarity between the development of the h-CRN regions in ma-BN and the development of nanocrystallites in MAC.

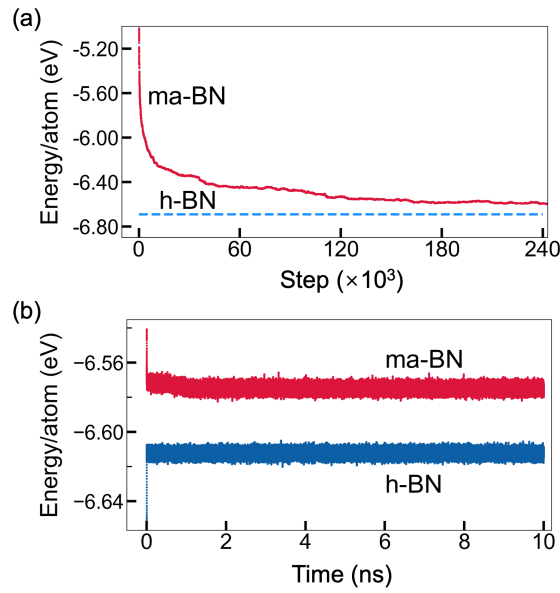


Fig. 2. The stability of ma-BN. (a) Energy evolution in the kMC simulation. (b) Energy evolutions in the classical MD simulations at 300 K for 10 ns. After reaching equilibrium, the energy fluctuates regularly with amplitude of ~ 10 meV/atom.

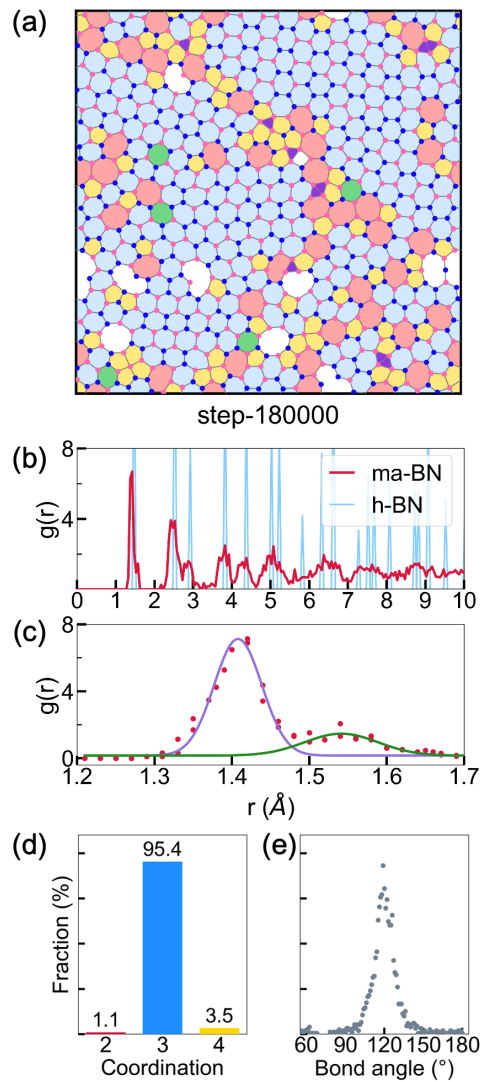


Fig. 3. Structural analysis of ma-BN. (a) A typical snapshot of ma-BN at equilibrium stage. (b) RDF plot of ma-BN compared with h-BN. (c) Zoom-in plot of the first peak of RDF. (d) The counting of coordination number of the (a). (e) Bond angle counting of (a).

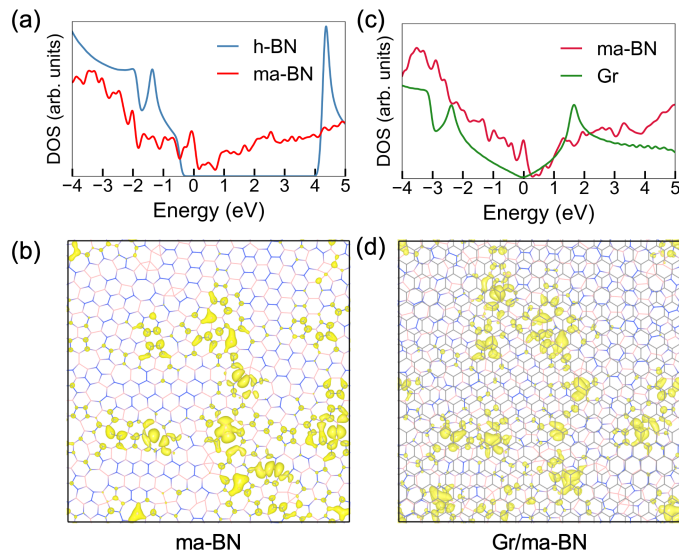


Fig. 4. Electronic properties of ma-BN and Gr/ma-BN. (a) Calculated DOS of ma-BN and h-BN. The Fermi energy is at 0 eV. (b) Charge density distribution of ma-BN near the Fermi energy in real space in the energy range $E_f \pm 0.2$ eV. (c) Calculated DOS of a Gr/ma-BN heterostructure. (d) Charge density distribution in real space of states of Gr/ma-BN in the energy range $E_f \pm 0.2$ eV.

Supporting Materials for
“The amorphous-structure conundrum in two-dimensional materials:
Monolayer amorphous carbon *versus* boron nitride”

Yu-Tian Zhang (张雨田)^{1#}, Yun-Peng Wang (王云鹏)^{2#}, Xianli Zhang (张现利)¹,
Yu-Yang Zhang (张余洋)^{1,3*}, Shixuan Du (杜世萱)^{1,4}, Sokrates T. Pantelides^{5,1}

- 1 University of Chinese Academy of Sciences and Institute of Physics, Chinese Academy of Sciences, Beijing 100049, China
- 2 Hunan Key Laboratory for Super Microstructure and Ultrafast Process, School of Physics and Electronics, Central South University, Changsha 410083, China
- 3 CAS Center for Excellence in Topological Quantum Computation, University of Chinese Academy of Sciences, Beijing 100049, China
- 4 Songshan Lake Materials Laboratory, Dongguan, Guangdong 523808, China
- 5 Department of Physics and Astronomy and Department of Electrical and Computer Engineering, Vanderbilt University, Nashville, Tennessee 37235, USA

Methods

The kinetic Monte Carlo simulations

Fully-tested kinetic Monte Carlo (kMC) simulations [1,2] are employed to obtain the atomic configurations of MAC and ma-BN. The kMC evolution corresponds to an annealing process [1,3,4]. Its validity was established in the simulation of MAC [3] and the successful reproduction of nanocrystallites in MAC in this study. Besides a reliable structural evolution algorithm, a suitable empirical potential is also necessary for correctly capturing the physical process in the formation of an amorphous material. To describe the interatomic interactions, we employed the adaptive intermolecular reactive empirical bond-order (AIREBO) potential by Stuart [5] for MAC, and the extended Tersoff potential for BN (BN-ExTeP [6]) for ma-BN, as implemented in the molecular dynamics code LAMMPS [7].

Specifically, BN-ExTeP is able to deal with variable coordination environments and give correct coordinations for both boron and nitrogen atoms [6], as we confirm in Fig. S2a. BN-ExTeP not only gives correct formation and binding energies in pristine and defected h-BN, but it is also capable of describing Stone-Wales and antisite defects in h-BN [6], which are exactly the two kinds of kMC operations we consider. For exchange (EX) and Stone-Wales rotation (SW), we further set up a series of benchmarks to compare BN-ExTeP with DFT. The noncanonical-bond energies are high in both methods (Table S2), indicating that BN-ExTeP does not bias noncanonical bonds with low energies. The phase separation energies are also high enough to prevent the

formation of borophene and N_2 molecules (Fig. S8). The SW/EX operations also show a consistent trend in both methods (Table S1). A reax force field (Pai et al, 2016) was also tested to give additional evidence of the CRN nature of ma-BN (Fig. S9).

For both MAC and ma-BN, the size of the supercell in the x-y plane is $45\text{\AA} \times 45\text{\AA}$, which is large enough to capture the ensemble fluctuations of a disordered system. The z-direction is separated by a 20\AA vacuum layer to diminish the interaction between periodic replicas. 772 carbon atoms and 744 boron and nitrogen atoms are randomly placed in the initial unit cell, respectively (Fig. 1a and 1e). The B:N ratio is 1:1, and the densities of atoms are kept the same as in the crystalline graphene and h-BN, respectively. During the kMC simulation, Stone-Wales transformations are performed for MAC. Considering the binary nature of ma-BN, both Stone-Wales and anti-site transformations (exchange two atoms) are considered. The structures are then relaxed by LAMMPS and accepted by a probability defined as $\min\{1, \exp[-(E_{\text{new}}-E_{\text{old}})/k_B T]\}$, where E_{old} is the energy of the current configuration, E_{new} is the energy of the new configuration, and $k_B T$ is set to 0.5 eV (k_B is the Boltzmann constant). It should be emphasized that the corresponding temperature of 5798 K has no physical meaning, but a reference meaning in the kMC method [1]. More than 200,000 kMC iterations are performed to ensure complete convergence.

Classical molecular dynamics. Classical MD implemented in LAMMPS is used to study the thermodynamic stability. This method is widely used in calculations for 2D materials [8,9]. The empirical potential for ma-BN and monolayer h-BN is BN-ExTeP. The 180,000th step representative kMC snapshot of ma-BN is chosen as the initial configuration for classical MD, and it is put in a NPT ensemble for structural relaxation at 300 K. The simulations of both ma-BN and monolayer h-BN are run for 10 ns, which is sufficiently long to capture possible structural changes and energy fluctuations.

DFT calculations. The Perdew-Becke-Ernzerhof (PBE) functional is used for exchange and correlation [10], as implemented in the VASP code [11]. The interatomic strain is released by DFT structural relaxation at first, until the net force is less than 0.1 eV/ \AA . In the Gr/ma-BN heterostructure, the interlayer distance is optimized by considering van der Waals interactions within DFT-D3 scheme [12]. Thereafter, the densities of states (DOS) are calculated with a converged k -point mesh of $5 \times 5 \times 1$. In Fig. 4, the charge density of ma-BN and Gr/ma-BN are integrated in an energy range of $[E_f - 0.2, E_f + 0.2]$ eV, where E_f is the Fermi energy. The iso-surface is set to 0.003 e/Bohr³.

Table S1. SW/EX rotation energies comparison between LAMMPS and DFT. In order to assess the agreement between LAMMPS classical MD and DFT, we compare the most typical SW/EX rotation energies in these two methods. A medium size supercell ($22 \times 22 \text{ \AA}^2$) is constructed for an independent kMC simulation. The smaller size is chosen to make corresponding DFT calculations feasible. Twenty accepted kMC snapshots with increased B-N bonds after the operation are picked up from this kMC simulation. The change of the B-N bonds are listed in the third column. The SW/EX operation energies are then compare between DFT and LAMMPS, which shows good statistical agreement. Negative energies in the table mean that, after an operation, the new structure has lower total energy, while positive energies mean that the new structure has higher energy. Among 20 energy data, 6 of them show different signs in the LAMMPS and DFT results, as colored in red. At first glance, this should give a statistical agreement of 70%. Note that classical MD and DFT have altogether different foundation, whereby 70% average agreement is satisfactory. Detailed inspections show that, there are one and five positive energies for LAMMPS and DFT, respectively. The five additional positive energies in DFT do not indicate a disagreement. As the acceptance probability is $\min\{1, \exp[-(E_{\text{new}}-E_{\text{old}})/k_B T]\}$, kMC may accept the structure with positive energy difference as well. It is likely that the additional five operations with positive energies in DFT may also be accepted by kMC. Therefore, the aforementioned 70% agreement is a lower bound.

step-	operation	$\Delta\text{num(B-N)}$	LAMMPS ΔE (eV)	DFT ΔE (eV)
4	SW	1	-9.218	-17.230
34	EX	1	-2.410	-5.884
50	SW	1	-0.508	-13.052
118	SW	2	-6.067	+2.006
192	EX	3	-7.692	+2.516
306	EX	2	-2.978	-1.263
422	EX	1	-0.885	+13.438
556	SW	2	-0.362	-10.549
744	SW	4	-2.166	-6.920
1,000	SW	2	-1.883	+0.982
1,599	EX	1	+2.185	+1.229
3,517	EX	2	-0.338	-3.537
4,008	EX	3	-2.145	-4.258
5,331	EX	2	-0.661	-0.357
7,032	EX	2	-0.070	+0.018
11,769	SW	2	-1.092	-1.432
15,603	EX	2	+0.365	-5.129
20,230	EX	2	-0.630	-1.047
32,156	EX	4	-1.143	-7.962
56,293	SW	2	-2.333	-1.636

Table S2. Noncanonical bond energies in h-BN. A $20 \times 20 \text{ \AA}^2$ h-BN supercell is constructed, and several EX/SW rotations are performed (shown in first column) to introduce noncanonical bonds. The number of noncanonical bonds are listed in the second column. By comparing LAMMPS and DFT, The energy trend is qualitatively consistent, as the noncanonical-bond energies are comparable in DFT and LAMMPS. However, the energies are fairly high. Nevertheless, the consistency between DFT and LAMMPS shows that the BN-ExTeP potential does not bias the noncanonical bonds with low energy cost. Instead, even with the fairly high noncanonical-bond energies, no h-BN crystallites form in ma-BN, which indicates that CRN is indeed an intrinsic feature of ma-BN.

ΔE (eV)/bond	num(bond)	LAMMPS	DFT
EX-1	4	2.04	1.89
EX-5	20	1.83	1.77
EX-15	60	1.10	1.60
SW-1	4	1.62	1.37
SW-5	20	2.56	3.07
SW-15	60	2.04	1.35

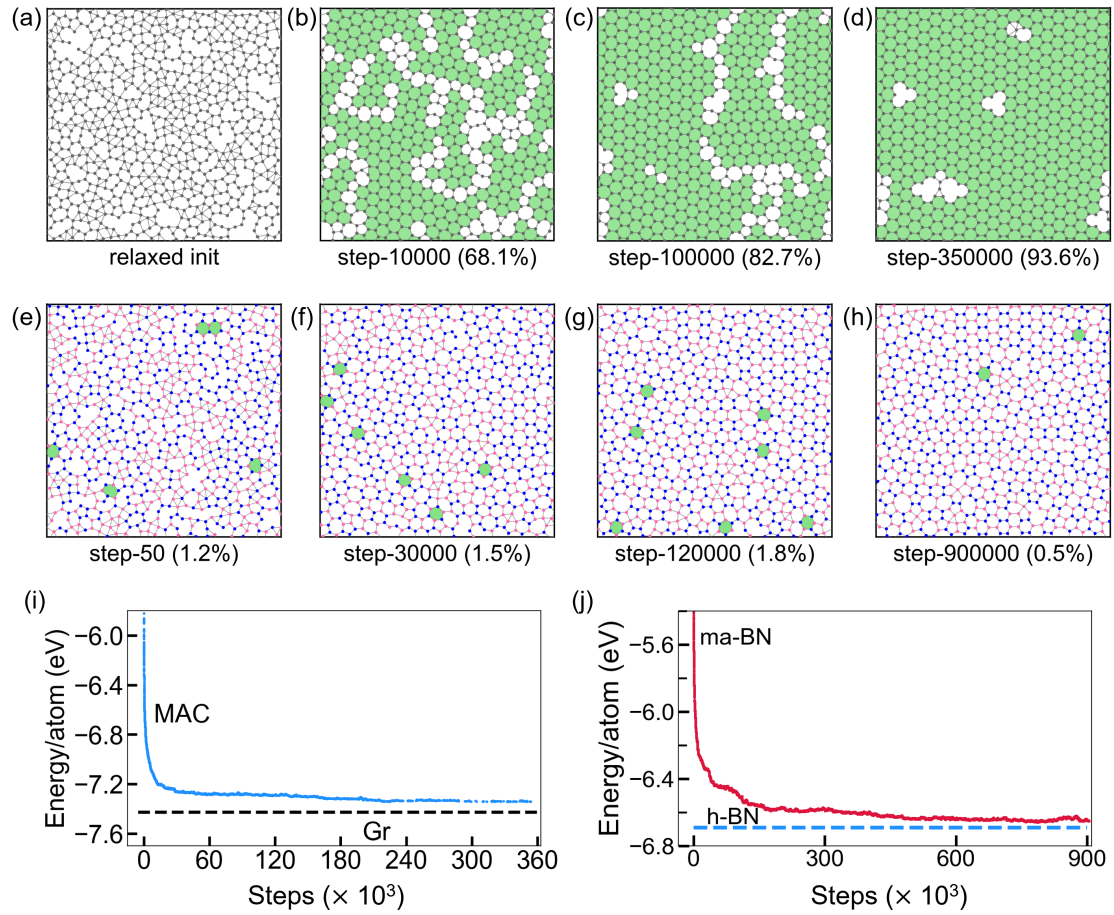


Fig. S1. Crystallite MAC versus CRN ma-BN. Canonical hexagons are colored green, and their percentages are listed in parentheses. (a) – (d) Four snapshots of MAC at different stages in the kMC simulation. (a) Initial stage. (b) – (c) Middle stage. (d) Final stage. Note that monovacancies persist after very long kMC annealing from panel (c) to panel (d). (e) – (h) Four snapshots of ma-BN at different stages in the kMC simulation. (e) Initial stage. (f) Middle stage. (g) equilibrium stage. (h) Long-time post-equilibrium stage. Canonical BN hexagons make up a negligible percentage in the entire kMC simulation, as they appear and disappear randomly. (i) The energy evolution of MAC compared with the energy of graphene. (j) The energy evolution of ma-BN as compared with the energy of h-BN.

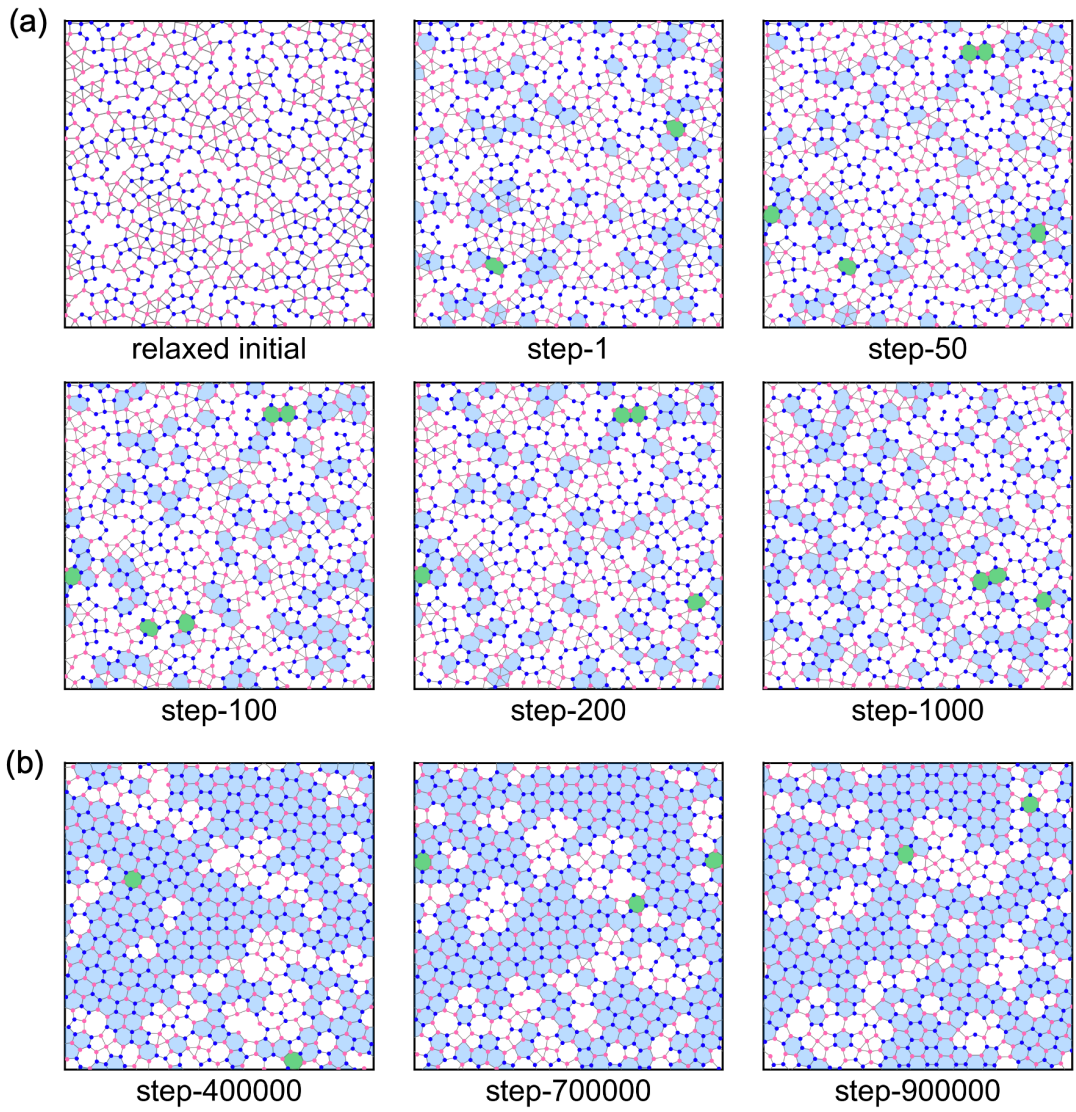


Fig. S2. The detailed kMC evolution of ma-BN. (a) Six snapshots in the initial stage. There are plenty of 2 – 6-fold coordinated boron and nitrogen atoms. These results indicate that the BN-ExTeP potential is capable of describing multi-coordinated atoms. Moreover, it means that the threefold coordination and the rapidly forming h-CRN islands are not pre-determined at the initial stage. Instead, their formation results as a consequence of energy competitions, which are controlled by the relative bond energies of B-N and noncanonical bonds encoded in the BN-ExTeP potential. (b) Three snapshots in the long-time post-equilibrium stage. The number of noncanonical BN hexagons (colored blue) saturates, and the number of canonical BN hexagons (colored green) cannot grow. The whole structure of ma-BN remains Z-CRN.

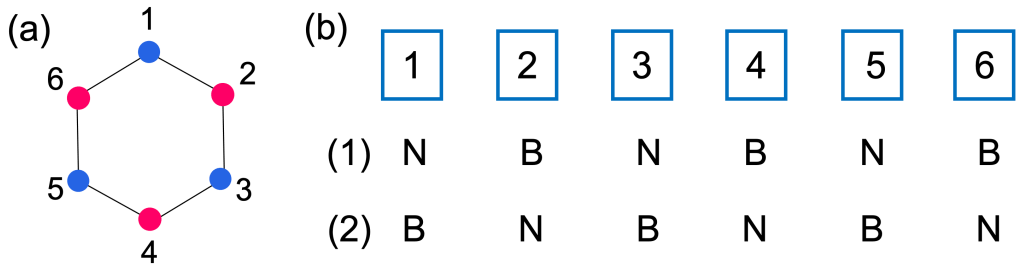


Fig. S3. The bonding probability of forming a canonical BN hexagon. (a) Schematic of a canonical BN hexagon ring. Red and blue dots represent boron and nitrogen atoms, respectively. (b) Estimation of the bonding probability in a setup scenario. We first consider the simplest case, which contains three boron atoms and three nitrogen atoms in a space. These six atoms can form bonds randomly with each other. Then the geometrical arrangement of these six atoms is confined in a hexagon ring, which can be mapped to a line-style arrangement as shown in (b). By a statistical analysis, each atom can occupy one of the six boxes at one time. The total possible arrangements is $6! = 720$. The probability of forming crystalline B-N alternated arrangements (canonical BN hexagon) is: $2 \cdot (C_3^1 \cdot C_3^1 \cdot C_2^1 \cdot C_2^1 \cdot C_1^1 \cdot C_1^1)$, where the factor 2 represents the two possible arrangements as shown in case (1) and (2) of Fig. S2b, and C_n^m represents the combination number of selecting m elements from n different elements. Therefore, the final probability of generating a canonical BN hexagon is $p = \frac{2 \cdot (C_3^1 \cdot C_3^1 \cdot C_2^1 \cdot C_2^1 \cdot C_1^1 \cdot C_1^1)}{6!} = \frac{1}{10}$. We must emphasize that, $\frac{1}{10}$ is just an upper bound of the real situation. In a CVD synthesis, there should be $\sim 10^{23}$ atoms in the ensemble, and they obey the same random bonding rule. As these atoms distribute randomly in the space, in a given next-nearest-neighbor radius, the probability to have exactly three boron and three nitrogen atoms is very low. Thus the probability of forming a canonical BN hexagon ring is even lower than $\frac{1}{10}$. This low probability prohibits the formation of h-BN crystallites.

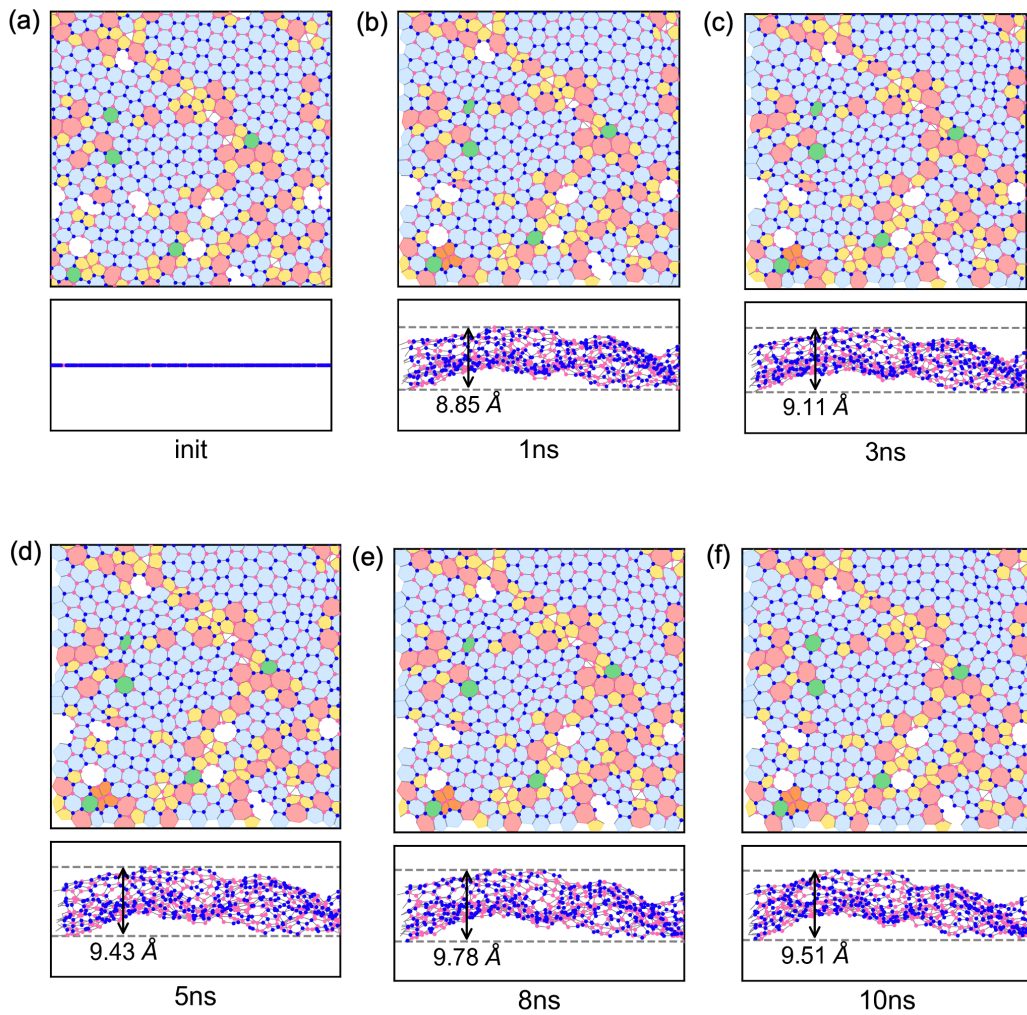


Fig. S4. Snapshots of ma-BN in the long-time classical MD in a NPT ensemble at 300 K. (a) Top and side view of the initial structure, which is the 180,000th snapshot from the kMC. (b) – (f) Top and side view of snapshots at middle and final stages in the MD simulation. The maximum thermal ripple is $\sim 9.5 \text{ \AA}$, much larger than 2.0 \AA of monolayer h-BN. This large out-of-plane displacement is caused by the amorphousness of ma-BN.

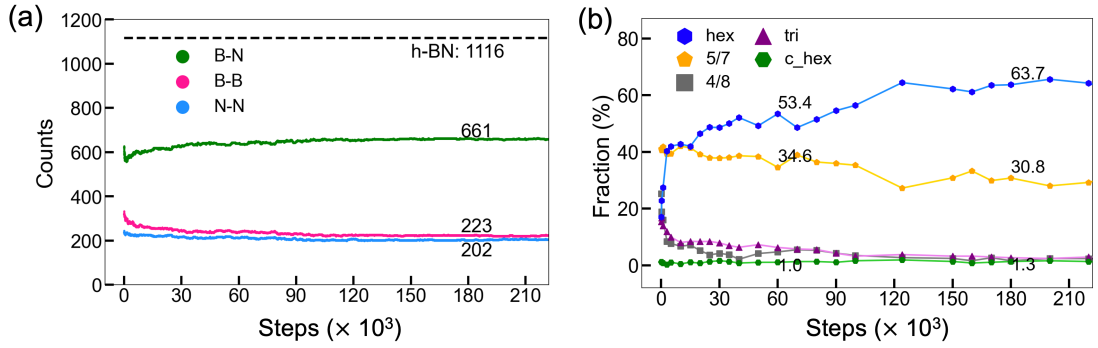


Fig. S5. The structural statistics in the kMC evolutions. (a) Bond-number counts during the kMC simulation. At the beginning of the evolution, three kinds of bonds experience sudden changes and then reach equilibrium at about the 120,000th step. The bond numbers at the 180,000th step are labeled. The number of B-N bonds is about 3 times of B-B and N-N bonds. We put the number of B-N bonds in a same-sized h-BN supercell (1116, black dashed line at the top) for reference. (b) Structural units counting during the kMC evolution. The crossover point of hexagons and 5/7 pairs is at about the 20,000th step. Thereafter, the hexagons become dominant and saturate at the 180,000th step.

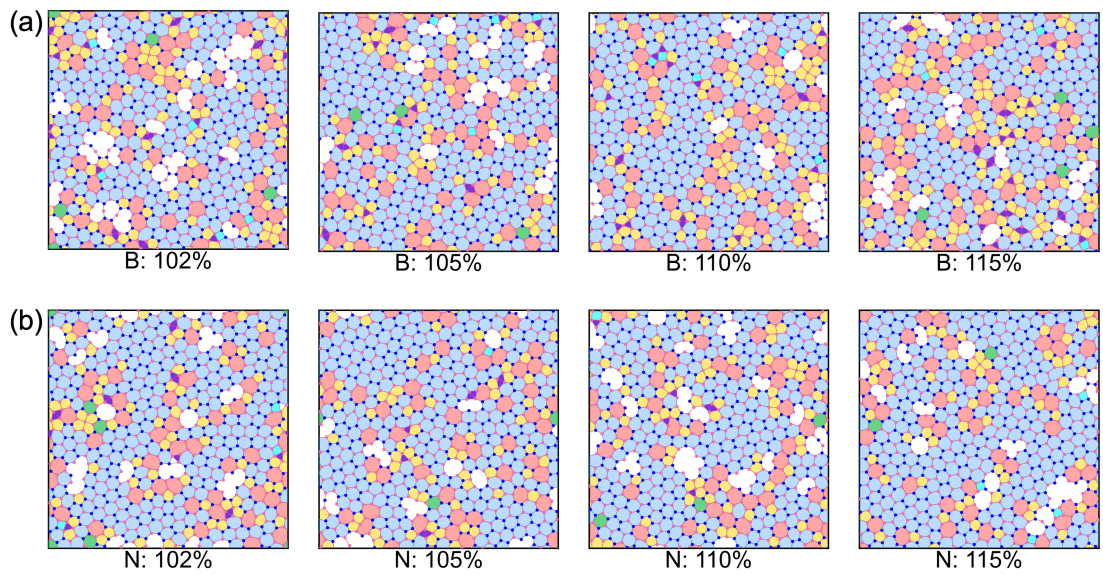


Fig. S6. ma-BN at different chemical stoichiometries. (a) ma-BN in a B-rich environment (B:N ratio from 102% ~ 115%). All the equilibrium snapshots are chosen at about 180,000th step of the kMC. The structure remains Z-CRN and no crystallites are observed. (b) ma-BN in a N-rich environment (N:B ratio from 102% ~ 115%), in order to simulate experimental N₂-rich growth conditions. The final structure of the kMC simulation still generates a Z-CRN. The slightly excess nitrogen does not eliminate the B₃ triangles, indicating that the B₃ triangle is an intrinsic, though rare, structural feature in ma-BN.

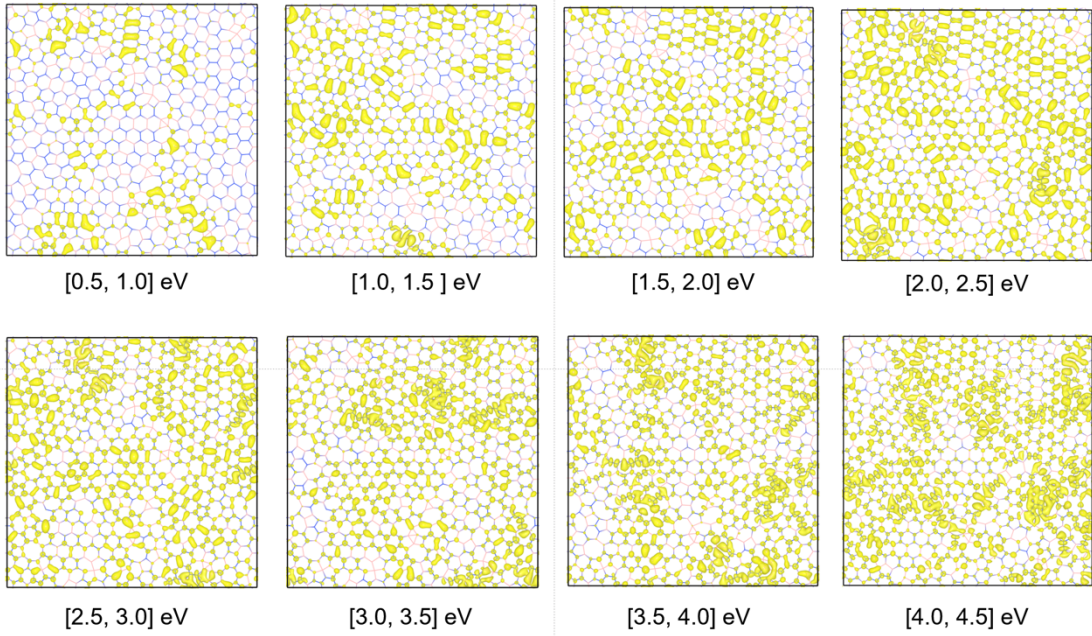


Fig. S7. Charge density distribution of ma-BN in real space at different energies. Isosurface is set to 0.003 e/Bohr³. Charge density distribution is integrated up to $E_f + 4.5$ eV, which is the gap range of monolayer h-BN in the PBE functional. The integration is performed with an energy window of 0.5 eV. The charge density is still localized and does not interconnect from E_f to $E_f + 4.5$ eV, suggesting that ma-BN is an insulator despite the absence of a true energy gap.

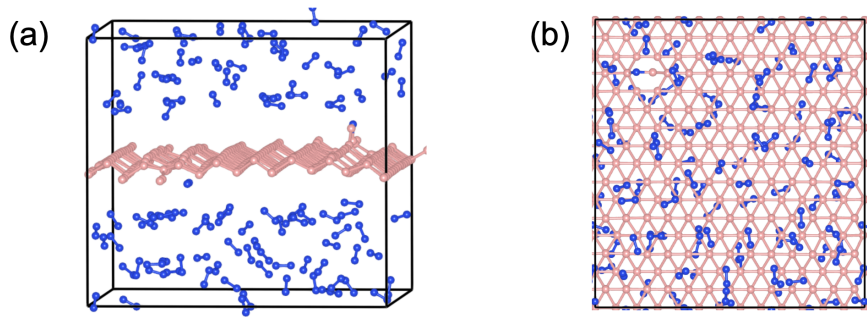


Fig. S8. The possibility of phase separation. (a) – (b) A perspective and top view of a configuration with a phase separation of borophene and N_2 gas. It is found that the formation of h-BN from a separated phase (borophene and N_2 gas) lowers the energy by 3.10 eV per BN pair at the DFT-PBE level, indicating that phase separation in the BN system is not likely. LAMMPS calculations give the same trend (3.29 eV per BN pair).

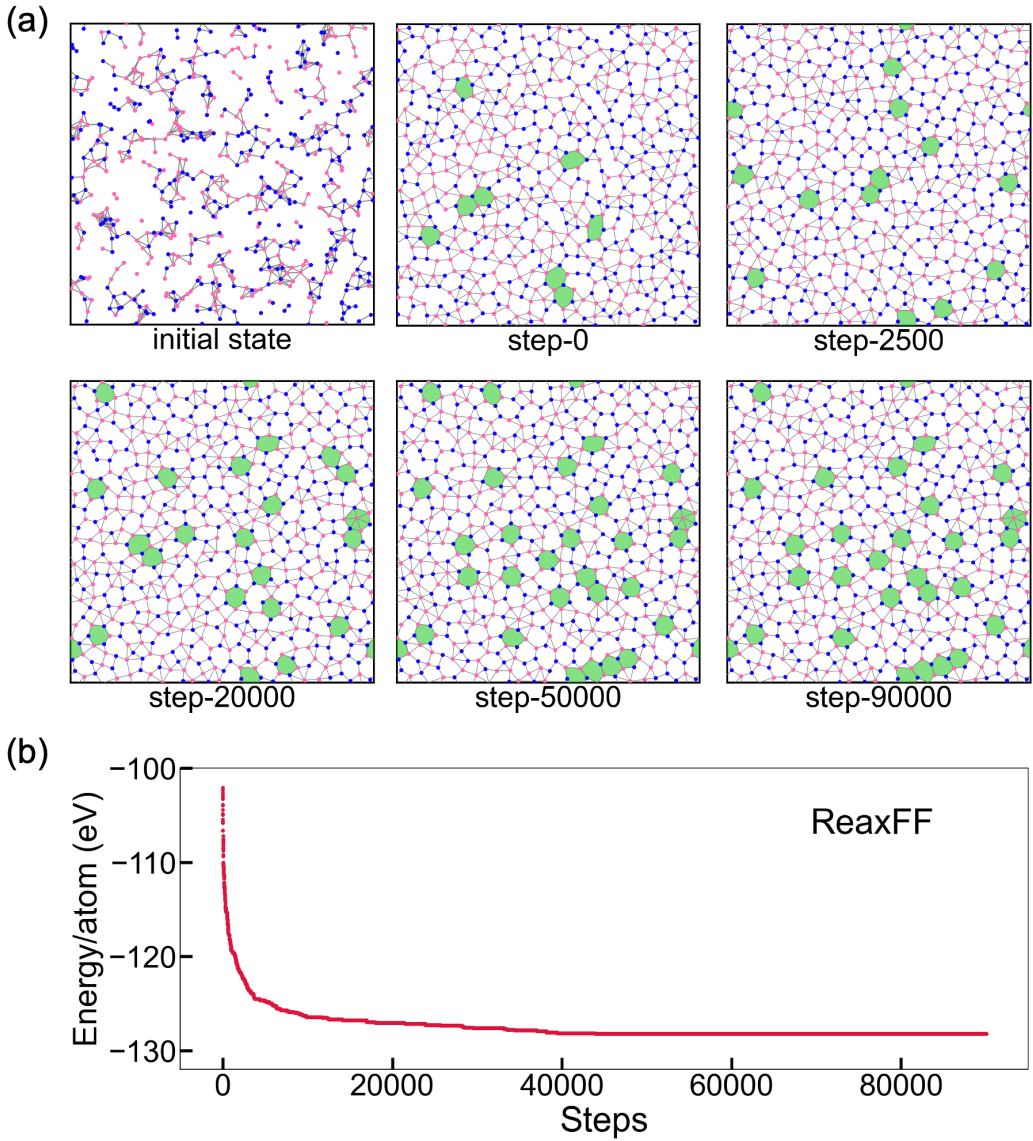


Fig. S9. The kMC snapshots of ma-BN in reax force field. The potential [13] is built to describe dehydrogenation reaction of liquid-phase CBN compounds, and was also employed to study the mechanical properties of borophene [14]. We suppose that this potential could give some qualitative description of disordered BN systems. Note that this simulation only has reference meaning, for the ReaxFF has not been fully tested in h-BN and lacks DFT comparisons. (a) Representative kMC snapshots. Starting from a random initial configuration, the atoms do not form any crystallites after reaching equilibrium. The net result is the same as obtained with BN Ex-TeP potential: ma-BN is a CRN. However, due to the different bonding characteristics of these two potentials, there are fewer noncanonical hexagons and more multi-coordinated atoms in ReaxFF. (b) Energy evolution in the kMC. The snapshot at the step 50,000 has reached equilibrium.

References

- [1] J. Zhuang, R. Zhao, J. Dong, T. Yan, and F. Ding, Evolution of domains and grain boundaries in graphene: A kinetic Monte Carlo simulation, *Phys. Chem. Chem. Phys.* **18**, 2932 (2016).
- [2] F. Ding and B. I. Yakobson, Energy-driven kinetic Monte Carlo method and its application in fullerene coalescence, *J. Phys. Chem. Lett.* **5**, 2922 (2014).
- [3] C. T. Toh *et al.*, Synthesis and properties of free-standing monolayer amorphous carbon, *Nature* **577**, 199 (2020).
- [4] W. J. Joo *et al.*, Realization of continuous Zachariasen carbon monolayer, *Sci. Adv.* **3**, e1601821 (2017).
- [5] S. J. Stuart, A. B. Tutein, and J. A. Harrison, A reactive potential for hydrocarbons with intermolecular interactions, *J. Chem. Phys.* **112**, 6472 (2000).
- [6] J. H. Los *et al.*, Extended Tersoff potential for boron nitride: Energetics and elastic properties of pristine and defective h-BN, *Phys. Rev. B* **96**, 184108 (2017).
- [7] S. Plimpton, Fast parallel algorithms for short-range molecular dynamics, *J. Comput. Phys.* **117**, 1 (1995).
- [8] Y. Ma, L. Kou, Y. Dai, and T. Heine, Proposed two-dimensional topological insulator in SiTe, *Phys. Rev. B* **94**, 201104 (2016).
- [9] W. Ding *et al.*, Prediction of intrinsic two-dimensional ferroelectrics in In_2Se_3 and other $\text{III}_2\text{-VI}_3$ van der Waals materials, *Nat. Commun.* **8**, 1 (2017).
- [10] J. P. Perdew, K. Burke, and M. Ernzerhof, Generalized gradient approximation made simple, *Phys. Rev. Lett.* **77**, 3865 (1996).
- [11] G. Kresse and J. Furthmüller, Efficiency of ab-initio total energy calculations for metals and semiconductors using a plane-wave basis set, *Comput. Mater. Sci.* **6**, 15 (1996).
- [12] S. Grimme, J. Antony, S. Ehrlich, and H. Krieg, A consistent and accurate ab initio parametrization of density functional dispersion correction (DFT-D) for the 94 elements H-Pu, *J. Chem. Phys.* **132**, 154104 (2010).
- [13] S. J. Pai, B. C. Yeo, and S. S. Han, Development of the ReaxFFCBN reactive force field for the improved design of liquid CBN hydrogen storage materials, *Phys. Chem. Chem. Phys.* **18**, 1818 (2016).
- [14] M. Q. Le, B. Mortazavi, and T. Rabczuk, Mechanical properties of borophene films: a reactive molecular dynamics investigation, *Nanotechnology* **27**, 445709 (2016).